Collimator Width Optimization in X-ray Luminescent Computed Tomography (XLCT)

Sourav Mishra

Thesis submitted to the faculty of the Virginia Polytechnic Institute and State University in partial fulfillment of the requirements for the degree of

Master of Science

In

Computer Engineering

Ge Wang

Jason Xuan

Guoqiang Yu

1 May 2013
Blacksburg, VA 24061

Keywords: X-ray Luminescence, Computed Tomography, Monte Carlo Methods

Collimator Width Optimization in X-ray Luminescent Computed Tomography (XLCT)

Sourav Mishra

ABSTRACT

X-ray Luminescent Computed Tomography (XLCT) is a new imaging modality which is under extensive trials at present. The modality works by selective excitation of X-ray sensitive nanophosphors and detecting the optical signal thus generated. This system can be used towards recreating high quality tomographic slices even with low X-ray dose. There have been many studies which have reported successful validation of the underlying philosophy. However, there is still lack of information about optimal settings or combination of imaging parameters, which could yield best outputs. Research groups participating in this area have reported results on basis of dose, signal to noise ratio or resolution only.

In this thesis, the candidate has evaluated XLCT taking into consideration noise and resolution in terms of composite indices. Simulations have been performed for various beam widths and noise & resolution metrics deduced. This information has been used in evaluating quality of images on basis of CT Figure of Merit & a modified Wang-Bovik Image Quality index. Simulations indicate the presence of an optimal setting which can be set prior to extensive scans. The conducted study, although focusing on a particular implementation, hopes to establish a paradigm in finding best settings for any XLCT system. Scanning with an optimal setting preconfigured can help in vastly reducing the cost and risks involved with this imaging modality.

For Priyanka

You are all my reasons.

ACKNOWLEDGEMENTS

I wish to express my heartfelt thanks to my advisory committee: Dr. Ge Wang, Dr. Jason Xuan and Dr. Guoqiang Yu. Without their support, I wouldn't have been able to make strides in research towards finishing a successful Masters in Science. My special thanks to Dr. Wang for his patience and understanding in guiding me towards my goals. I have been fortunate to work with him on Multi-Scale CT and X-Ray Luminescent CT. Apart from gathering technical skills I have learnt few important lessons in research from him – to never give up & always give a helping hand. These will be invaluable companions in the years to come. I am also very thankful to Dr. Guillem Pratx for his insightful guidance in helping me design the simulations.

My gratitude also goes to Suvojit, Aditya & Ravi. Thanks to the endless sessions of discussions, I have learnt a lot from you both. Working with you has been a pleasure and I am eternally thankful for having listened to all my queries – both silly and profound. Siddharth and Alokika deserve warm thanks for being there whenever I had to unreasonably complain about workload. I couldn't have finished successfully without their encouragement.

The most special thanks go for Mom and Dad. Thanks for believing in me and standing by my side, even when I wasn't sure about myself. I couldn't have been successful without your prayers and blessings. I have come a long way from scribbling alphabets on a slate to writing engineering equations. I want to let you know that it is all because of you.

TABLE OF CONTENTS

LIST OF FIGURES

LIST OF TABLES

LIST OF REPRESENTATIVE SIMULATION OUTPUTS

INTRODUCTION

NANOPHOSPHORS FOR XLCT

The first step towards envisioning a Computed Tomography modality based on X-ray luminescence could be traced to the research & development of novel coordination complexes and unique inorganic materials. These substances are capable of emitting visible and Near-Infra Red (NIR) photons when exposed to high energy beams of radiation. Although, phosphors which were iridescent to X-ray energy existed for several decades, they were being primarily used in screens meant to planar, radiographic imaging. They had low quantum yield and usually were utilized in conjunction with a photo-multiplication tube (PMT). Standalone chemicals which were capable of producing sufficient yield of radiance didn't exist until about two decades ago.

A monumental publication in 1996 paved the way for making substances with high photo-conversion efficiency. In a publication with *Science*, nanoparticle clusters were proposed to significantly improve the quantum yield [1]. Research until then had focused on the chemical properties of materials – fragments of semiconductors consisting of scores of atoms. Traditionally, efforts had aimed at increasing efficiency by various schemes of doping and tempering the material, but not on the physics of clusters. The research carried out by the A.P. Alivisatos at University of California, Berkeley, established that aggregating nanoparticles in some specific geometry proved a better technique in improving efficiency. Further, this research also highlighted the fact that nanoparticles exhibit size-dependent optical properties, often non-linearly increasing with increasing size of clusters. Super-lattices made from individual units had quantum yields several folds higher than individual nanoparticles. This exciting find led to several similar publications with a variety of other materials.

Inert, photo-stable and biocompatible nanoparticles, suitable for long-duration *in-vivo* imaging were successfully synthesized only about a decade later. In a review publication in *Small*, W. Cai and X. Chen brought together and published relevant nanophosphor chemistry, several of them useful towards X-ray based small animal imaging [2]. The families of Nano-materials promulgated by the paper helped in setting the directions for the right class of compounds for use in several modalities. The review publication also emphasized on making the Nano-platform inert during delivery, by use of Zn-S coating. Nano-platform based research was until then, limited to vasculature related studies. This publication, along with few others emerging shortly thereafter, set the motion for application of Nanophosphor for a wide variety of CT applications [3, 4]. Cameras sensitive to both optical and NIR light were already available commercially c. 2000. Suitability of phosphors paved the way for designing a system, based completely on novel properties of X-ray Luminescent materials. Table 1 lists the broad class of Nano-platforms which have evolved over time for different modalities.

Nano-platform	Composition	Imaging Modality
Quantum Dot	Doped CdTe, CdSe	Optical Fluorescence
Nano-shell	Au	OCT
Bi_2S_3 Nanoparticles	Doped Bi_2S_3	CT
Iodinated Nanoparticles	I	CT
SPIO, CLIO	Fe oxides	MRI
MNMEIO	Mn, Fe Oxides	MRI
PFC	F, C based nanostructures	Label dependent

Table 1: Nano-platforms & Modalities
(Shen et.al, *Small,* v. 3(11) 2007, Under Fair use 2013)

Nanophosphor specific to X-ray Luminescence scheme in CT was soon introduced by few independent groups. In a publication with *Journal of Alloys & Compounds* in 2007, Ying Tian et.al, proposed and characterized nanoparticles which were strongly X-ray Luminescent [5].

They identified doped Gd_2O_2S as a suitable candidate because of a high efficiency in converting X-rays to visible light. This was beneficial from the aspect of creating and operating a practical imaging system. The photon conversion efficiency being directly dependent on the particle size & morphology, they chose complex precipitation methods over solid-state reactions. In the solid state methodology, intermediate steps such as raw material blending, high temperature calcination, washing, milling and filtering introduced unavoidable impurities and caused inhomogeneity. The end product was of reduced light efficiency. To eliminate time-consuming and error prone steps, complex precipitation was adopted. This new method was capable of producing homogenous spherical particles of high purity and efficiency. Moreover, the method was also both time and cost efficient. Doping the material with Europium or Terbium was precise and easy. The size of nanoparticles, which was dependent on the milling process previously, could be controlled by the concentration of reactants and time of production.

In the method proposed by Tian et.al, a certain amount of $NH_4HCO_3(AR)$ powder was dissolved into $NH_3.H_2O(AR)$ solution and stirred vigorously to obtain the complex precipitant solution. The concentration of $NH_4HCO_3(AR)$ and $NH_3.H_2O(AR)$ were set as per requirements. Weighed Nitrate solutions of rare earth $Gd(NO_3)_3$ & $Tb(NO_3)_3$ were mixed, with doped concentration of activator Tb^{3+} carefully monitored. The complex precipitant was dropped into the nitrate solution slowly and with constant stirring for about 30 min and allowed to settle for ~2 hours. The reactions could be described in the following way.

The rare earth (designated Re) joined the reaction as,

$$\mathrm{Re}^{3+} + yCO_3^{2-} + xOH^- + nH_2O \rightleftharpoons \mathrm{Re}(OH)_x(CO_3).yH_2O$$

The resulting precipitate was centrifuged washed and ultrasonically dispersed before drying. $Gd_2O_2S{:}Tb$ Phosphor particles were obtained by calcination of $\mathrm{Re\ OH}_x\ \mathrm{CO}_3$ at a high temperature (900-1100 Celsius). X-ray diffraction studies (Fig. 1) showed that phosphors were relatively pure and in a hexagonal arrangement (Fig. 2). This appeared a good indicator of the purity, uniformity and mono-phasic nature of particles.

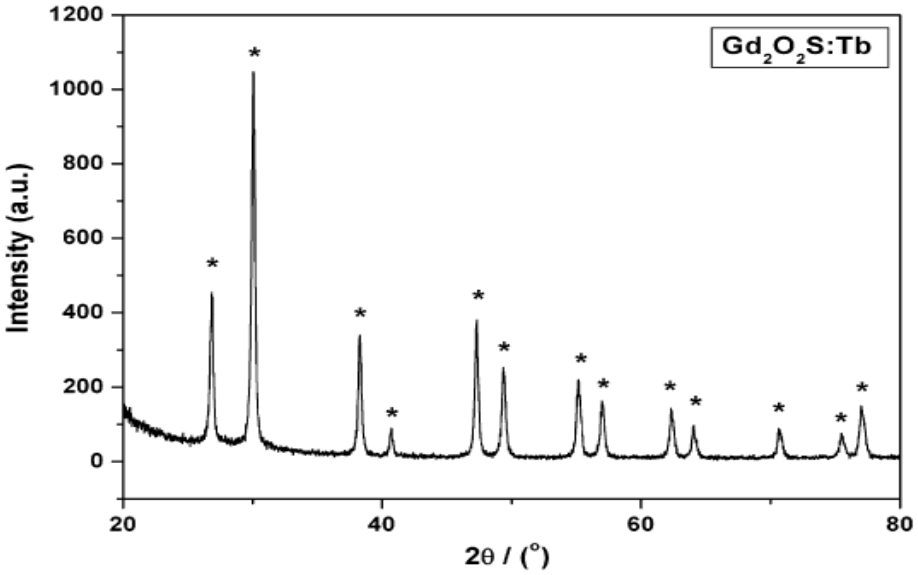

Figure 1: X-ray Crystallography showing characteristic peaks for Gd_2O_2S
(Tian et.al, *J. Alloys & Comp. v. 133(1-2), 2007, Under Fair use 2013)*

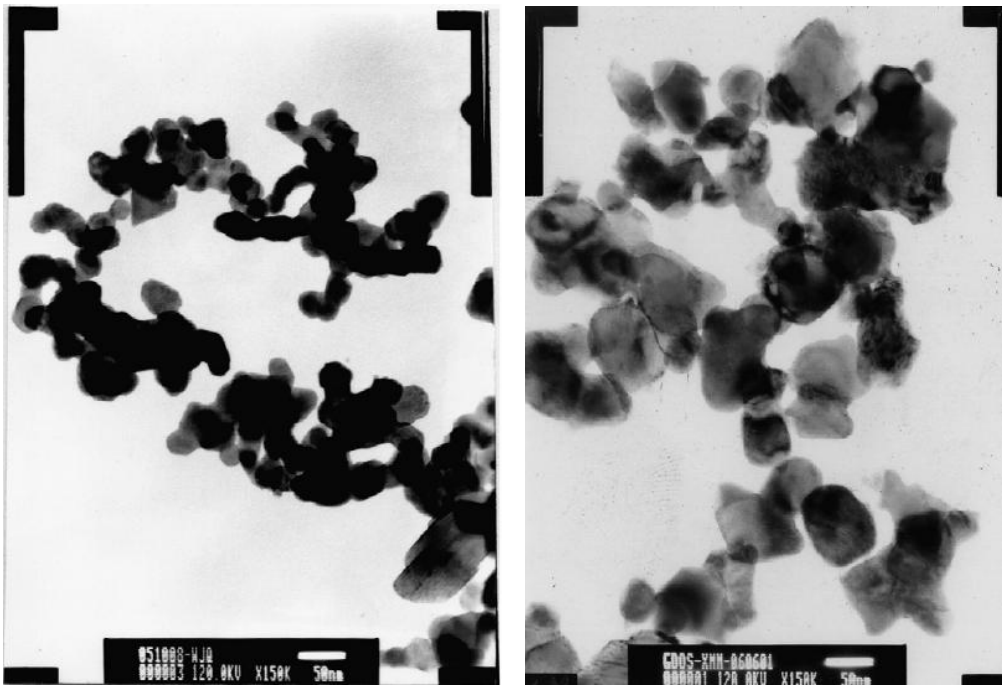

Figure 2: TEM Image of XL Nanophosphor
(*Left:* At 900^0C *Right:* 1100^0 C Sinter. Tian et.al, *J. Alloys & Comp, 2007,Under Fair use 2013)*

Transmission Electron Microscopy (TEM) verified quasi-spherical shapes of the phosphor. The size of the particles could be controlled by the temperature of sintering, with median range being 35-70 nm. The prepared phosphor was capable of emitting bright green light of sufficient luminescent intensity, exhibiting the characteristic peaks of Tb^{3+}. Results from an improved technique, creating mono-dispersed Gd_2O_2S: Tb nanoparticles were published by Ming et.al, in *Chinese Science Bulletin* in 2009. It saw a dramatic scaling (up to 50%) in the luminosity of nanophosphor by a refined precipitation-crystallization process [6]. Phosphor preparation has become reliable over the time and extends to improve efficiencies by introducing different dopants & varying concentrations. Common additives are Terbium (Tb) and Europium (Eu).

PHYSICS OF X-RAY LUMINESCENT NANOPHOSPHOR

When X-rays interact with matter, a variety of processes in geometrical and physical optics are found to occur. The physical effects are absorption, elastic scattering and inelastic scattering. We are concerned only with absorption of energy within crystal lattices, when we investigate X-ray luminescence. The absorbed energy in the lattice is returned in form of Fluorescence and Luminescence, depending on the form of crystal in use. Luminescence and Fluorescence both emit light but the physical phenomenon underlying both of them are slightly different [7].

Since the absorbed X-ray is responsible for emission of optical light, the phenomenon is more aptly called X-ray induced Optical Luminescence (XEOL). Luminescence which is observed from pure particles is called *intrinsic luminescence*, and the one induced by addition of dopants is called *impurity luminescence*[7]. The typical conversion efficiency for the phosphors are usually low (~ 15%) and the effects have been understood clearly only for halides, which are among the simplest of solid crystals. Compared to X-ray Fluorescence, the phenomenon is more sensitive and was originally developed to study rare earth minerals. Now the phenomenon has found application in medical technology field with the advent of X-ray Luminescent CT.

There are at least 3 broad stages which are believed to be responsible for conversion of the X-ray energy to visible light[8]. The first stage consists of absorption of X-ray energy into the crystal, primarily by photo-electric effect in the first 10^{-15} seconds. The next stage consists of the time interval between 10^{-15} and 10^{-9} seconds and results in the evolution of X-ray induced electron hole pairs in various deformities in the crystal. The ability to dislodge ions and create vacancies & interstitials by X-ray photons possessing negligibly small momentum is a phenomenon still

under research. During this stage, excitons, color centers and other defects aggregates are formed. In the third and the final stage, (10^{-9}s onwards), radiation induced defects choose one of these pathways.

- Recombine to form luminescence
- Remain as metastable color-centers
- Decay by irradiative process producing heat as a byproduct.

The first pathway, which is a fraction of all the processes happening, results in XEOL. The proportion of lattice centers undergoing deformation leads to the idea of quantum efficiency of the crystal. If more number of lattice points recombine, then quantum efficiency of the crystal is innately high and it would serve a good candidate to X-ray Luminescence based studies [7-9].

X-RAY LUMINESCENT COMPUTED TOMOGRAPHY

One of the earliest expositions, combining the knowledge of nanophosphors with Computerized Tomography came from Stanford University's Radiation Oncology Department, which put forward the idea, that conventional Computed tomography schemes could be put to use for molecular imaging through radio-luminescent phosphors. In a publication with *Optic Express* [10], G. Pratx et.al put forward the proposal that phosphor nanoparticles can be used in conjunction with traditional CT for useful anatomical and functional imaging techniques. They noted that Iodine and Barium Sulfate were capable of functional imaging with CT [with concentration > 1 mg. /ml], but more sensitive molecular agents were required for molecular imaging in the true sense. The authors discussed the unique properties exhibited by certain

nanophosphors which were capable of producing NIR light. These NIR light could propagate through the tissue and be measured by a sensitive photo-detector array. A single 100 KeV photon in many cases could liberate more than 5000 visible photons distributed around the primary ionization track. For dilute amounts of the Phosphor Nanoparticles (PNP), the light could be produced by X-ray interaction with tissue, since energetic electrons liberated from an active center could travel to nearby PNP's and produce luminescence. Signal measured was directly proportional to the concentration of phosphor nanoparticles in the region of interest and auto-fluorescence didn't compete with the measured signal. They theorized that X-ray Luminescence Phosphors could be used as emissive imaging probes. These nanoparticles could be excited by collimated X-ray beam from a CT & emitted light could be measured and reconstructed along the beam projection path. Competing auto-fluorescence was non-existent.

In a standard radiation exposure, the numbers of photons produced were few. Hence an accurate reconstruction by Bioluminescent Tomography scheme was limited. In X-ray Luminescence CT, *selective excitation* scheme was deployed. In such a scheme, the sample was to be irradiated by a sequence of narrow X-ray beams positioned at predefined locations. Regardless of where the photons are detected, it could be safely assumed that they originated somewhere along the path of the X-ray scheme[10]. Such an assumption greatly improved the reconstruction scheme and in many ways was equivalent to the first generation CT in design. In the journal communication, the authors reported XLCT images produced from 2 phantoms. These phantoms were fabricated by suspending Gd_2O_2S:Eu (GOSE) in 1% agar gel solution. The phosphor was suggested to be instrumental to proof of concept and not for *in-vivo* imaging. The phantom was a cylinder 1 cm in diameter and 2.5 cm high. Titanium Dioxide and India ink mimicked the optical properties of

biological tissues. Spectroscopic studies done on the phantom revealed the optical and scatters coefficient distribution in the phantom. The strongest signal at 630 nm exhibited an absorption coefficient μ_a = 0.025cm^{-1} & transport scatter coefficient μ_s'= 7.8 cm^{-1}. A gradient phantom was also designed consisting of eight 1 cm rods containing various phosphor concentrations inside a cylinder of 6.2 cm diameter and 4 cm height.

The X-ray was operated at 50 kV and 30 mA. The beam was filtered by 0.4 mm thick Aluminum plate. The phantom was translated 26 mm (1 mm increments) per view for 24 projections over 360 degrees. X-ray collimation was done by a 1mm spot. The resulting X-ray luminescence was recorded by an EM-CCD camera (Image-EM C9100-13, f/1.4, 512x512, δ=160, 1 second exposure). The hotspots formed by secondary X-rays were digitally removed by image processing techniques. The corrected images were used in *single-pixel* mode to reconstruct images. A brief schematic shown illustrates the experiment.

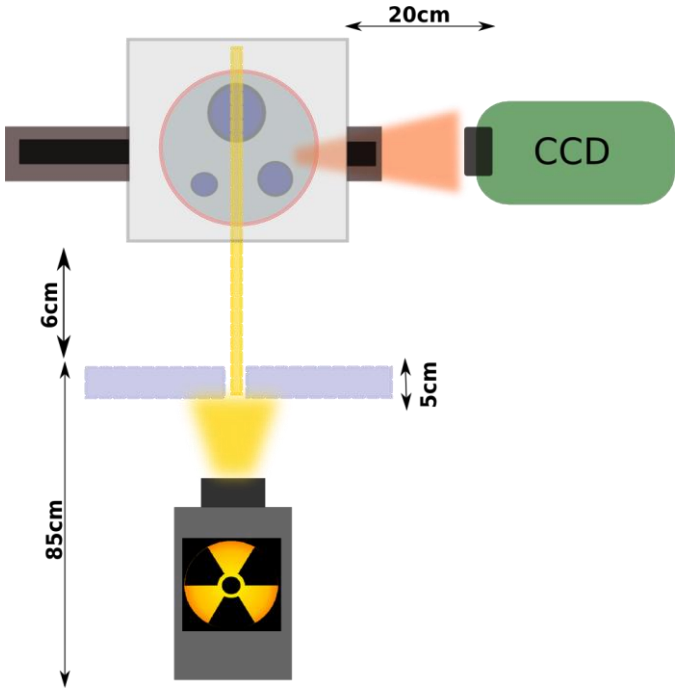

Figure 3: Proposed XLCT system for Tomographic Imaging

A rough correction was applied for a turbid phantom to compensate for exponential attenuation. Details of the correction have not been explicitly discussed. The sinogram from each phantom was reconstructed by ML-EM method. Assuming emission at 630 nm only and perfect quantum efficiency, computer simulations were also performed and images faithfully reconstructed from projection images. The following image shows a comparative study between actual and simulated image, exhibiting a high degree of accuracy between the two.

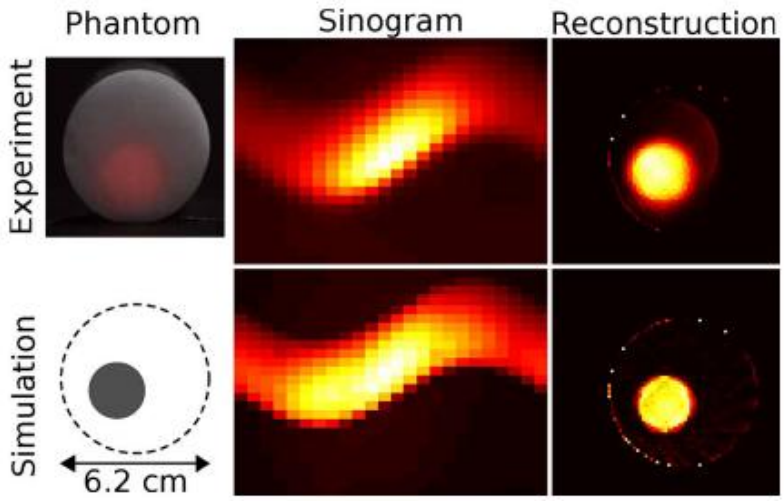

Figure 4: Comparison between experimental and simulation results
(G. Pratx et.al, *Optic Letters v. 35(20)*, 2010, Under Fair use 2013)

Through the experiments, it was established that optical signal had strong linear correlation with the amount or concentration of the nanophosphor. The correlation between simulated output and actual reading was found to be of very high order ($R^2 > 0.99$). The paper further noted that XLCT modality could be used for spatially and temporally registered images. An important note made with this publication was that beam width could play a vital role in optimizing the quality of images.

Using the conclusions drawn from the previous set of experiment, a new experiment was devised and published by the same research group [11]. The publication elaborated on previous experiment by stating the imaging model and reconstruction model in more details. A high energy Monte Carlo package was used in their experimental simulation to calculate the distribution of charges in the cylindrical phantom. Beam width and Energy was kept at 100KeV and 1mm respectively. Measurements were recorded for 50 positions over 64 angles covering 360^0. The experiment simulated $Gd_2O_2S:Tb$ with an emission wavelength of 802 nm. The experiment forayed into investigating a sensitivity phantom for nanophosphor rods having different concentrations, a lesion detectability phantom for non-specific uptake and a resolution phantom to evaluate various beam sampling patterns. X-ray transmission signal was reconstructed by Filtered Back projection (FBP) and a Shepp-Logan filter in the traditional CT scheme[12, 13]. Since a single-pixel mode was employed, the resolution of X-ray CT matched that of XLCT. Detectability of the sensitivity phantom was contingent on the dose of X-ray and amount of nanophosphor present. Smaller objects of interest were detected poorly owing to corruption of signal at detector and low amount of emission. However, larger objects could be well differentiated. Increasing the dose could completely resolve all the objects, irrespective of their sizes or nanophosphor concentration contained. It also increased the quantitative accuracy of the reconstruction. The lesion detectability phantom was well reconstructed with a high amount of dose and the quality degraded significantly when the dosage was reduced. These images were reconstructed through 50 iterations of the MLEM phantom. The Contrast to Noise ratio was calculated for various amounts of dose and the authors demonstrated that the ability to resolve contrast (CNR > 4) and detect objects was impeded with decreasing amount of dosage. When radiation dosage was not limited, it was possible to detect objects fairly well and the

resolution was as good as the transmission CT. The resolution phantom was also reconstructed by 50 iterations of the MLEM technique. Due to greater optical attenuation arising from the structure of phantom, accuracy was poor at the center of the phantom. Resolution was 1mm i.e. similar to transmission CT in the case of high dosage. The authors have emphasized that Noise and Resolution of the image was highly contingent on the dose of the X-ray, all other parameter kept the same and was the determining factor in the quality of image. The study lacked extensive insights into qualitative analysis of image quality however.

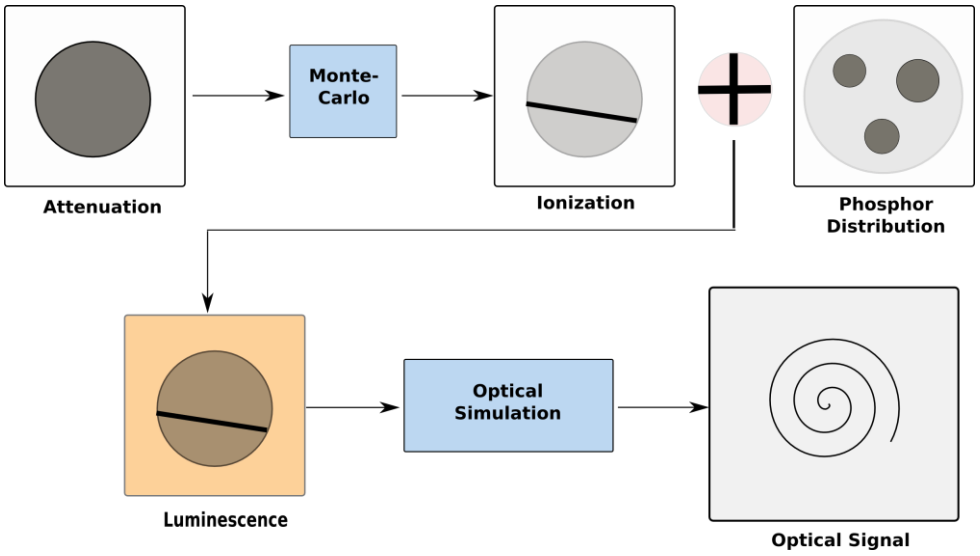

Figure 5*:* Flowchart of XLCT imaging process.

Concurrently, another publication by the same authors highlighted the advantages of using X-ray CT and X-ray Luminescent CT in tandem, producing fused images. The proposed dual modality system merged X-ray CT and XLCT. Practical aspects relating to phosphor concentration, light emission linearity, detector damage and spectral characteristics were studied. Contrast resolution as compared to X-ray Fluoroscopy was also studied towards this publication [14].

The paper reported numerical values for the dosage received by the CCD detectors. Recommendations from the paper reported that dose to CCD could be reduced to as little as 1.5 µGy if proper shielding was used. The dose to air in the vicinity of the camera in absence of the shield was measured to be 300 µGy, which had an adverse effect on the quality of signal detected over a prolonged use of the camera. However, determining a damage threshold was not realized in the study. The authors further noted that cumulative doses (over period of time) above 25 and 100Gy were to be considered thresholds for increased noise and detector damage. De-noising strategies could be employed via image processing techniques and digital filters to remove hotspots from the image which usually appeared as random pixels with intensity values very close to the maximum values.

Gd_2O_2S (GOS) doped with Tb was found to emit light at 545 nm and GOS: Eu gave spectral peaks at different wavelengths – 596, 618, 627 and 707 nm with the strongest signal at 627 nm. Studies on the linearity of light emission with respect to dose was done by two methods – (1) by keeping tube voltage constant and increasing the current from 5 mA to 20 mA & (2) keeping tube voltage and current constant and increasing the exposure time. Both current/dose and time/dose linearity were confirmed by running linear correlation analysis ($R=1$, $p<0.001$). Plots of photon counts detected compared to concentration of nanophosphor showed a linear relation in logarithmic scale. The paper made an important observation that when dose was kept low; nanophosphor concentration had to be increased significantly to get a good signal. This in turn could induce cellular toxicity. Higher doses of X-ray, in presence of lower concentration could also adversely affect the subject/specimen.

For detection at surface of tissue, X-ray mammographic doses were sufficient to locate Pico-molar concentrations of phosphor. At depths, higher doses were required. This method could be used in conjunction with radiation therapeutics. The higher dosage could effectively treat the patient as well as give accurate real-time information on the proliferation of the tumor, which could evade detection with conventional CT. The tracers were recommended to be imaged in the first 10-20 cGy.

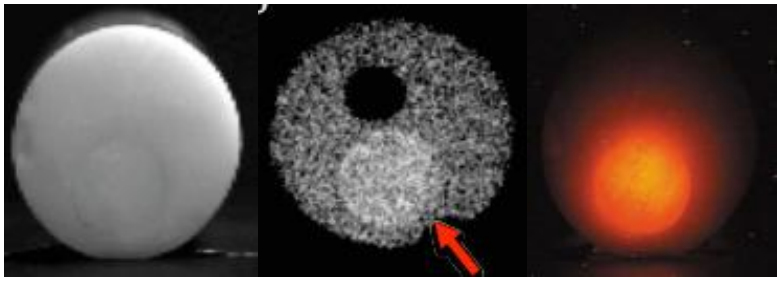

Figure 6:(L-R) Phantom, Projection Fluoroscopy & Optical emission.
(Carpenter et.al, Med. Physics 2010, Under Fair Use 2013)

The contrast in the case of XLCT was found to be 2.5 times higher than X-ray Fluoroscopy with the same amount of dose, even if it was considered that the light photons had scattered through the tissue before being detected. Using an efficient model to simulate the photon trajectory could hypothetically yield even higher contrast characteristics. A major advantage over X-ray fluoroscopy was stated to be the low quantity of tracer uptake required to produce higher quality image. At its best, the study reported a 430-fold improvement in contrast recovery for optical detection as compared to fluoroscopic detection.

A recent proceeding had aimed at implementing cone-beam X-ray Luminescent Computed Tomography [15]. Compared with narrow beam XLCT techniques, the method could utilize the

X-ray beam more efficiently. A major advantage would be dose reduction and scanning time shortening. The publication exhibits use of Diffusion Approximation (DA) to alleviate the ill-posed problem of optical scatter within specimen. In addition sparse regularization and incomplete variable truncation conjugate gradient (IVTCG) were used in reconstruction instead of algebraic techniques.

The authors had proposed a cone beam model based on the following schematic (Fig. 7). The experimentation was carried out via two pathways – *uncompensated* method, where X-ray beam intensity was considered unaltered and *compensated* method where Lambert-Beer's law was used to account for the reduction in X-ray intensity at the source of light.

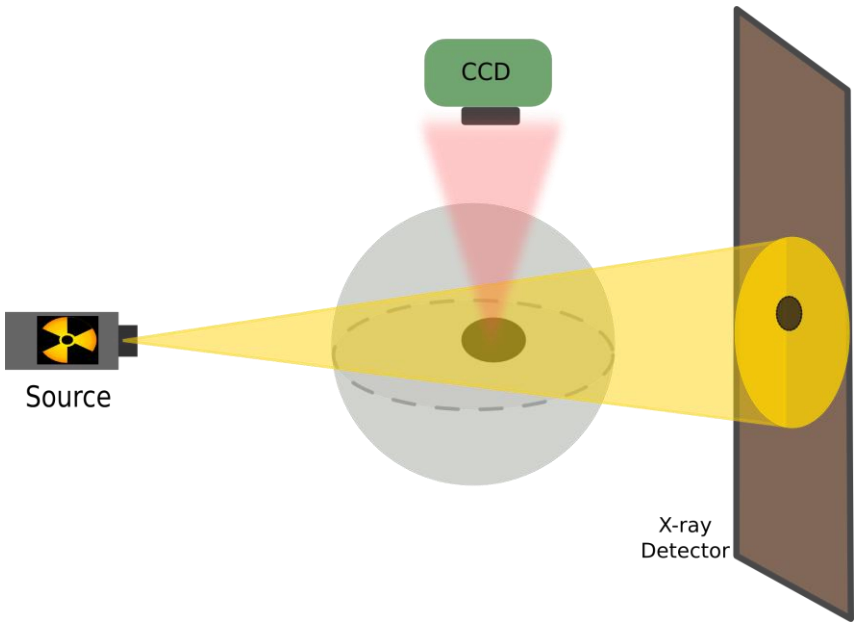

Figure 7: Schematic for proposed Cone-beam XLCT

Light transport in the biological tissue was modeled by Radiative Transport Equation (RTE) simplified to Diffusion Approximation and given as follows,

$$-\nabla\cdot[D(\mathbf{r})\nabla\Phi(\mathbf{r})]+\mu_a(\mathbf{r})\phi(\mathbf{r})=S(\mathbf{r}),\ \mathbf{r}\in\ \Omega \qquad (1\text{-}1)$$

The Diffusion constant D(**r)** in the equation was the following

$$D(\mathbf{r}) = {}^{1}\!\!\diagup\!\!{}_{3[\mu_a(\mathbf{r}) + (1-\mathbf{g})\mu_s(\mathbf{r})]} \tag{1-2}$$

Additionally, photon propagation with stable state diffusion was could be complemented by the Robin boundary condition given as,

$$\Phi(\mathbf{r}) + 2k(\mathbf{r}, n, n')D(\mathbf{r})[v(\mathbf{r}) \cdot \nabla\phi(\mathbf{r})] = 0, \ \mathrm{r} \in \partial\Omega \tag{1-3}$$

Where v(**r)** was the outward unit normal vector and **k** was the boundary mismatch factor. A finite element scheme was used to solve for the diffusion equations. For reconstruction, regularization techniques were used to solve the ill-posed problem. In the forward model based on finite element scheme, a matrix **M** could be defined which obeyed,

$$M \cdot \phi = \mathbf{F} \cdot \grave{\mathrm{o}} \cdot X \cdot \rho \tag{1-4}$$

ϵ was light yield; X corresponded to X-ray intensity at end vertices of the finite element and ρ the density. **M** could be considered positive definite and hence,

$$\Phi = A \cdot \rho, \ \text{where A=}(\mathrm{M}^{-1}\mathbf{F}) \cdot \in \cdot X \tag{1-5}$$

Equation 1.5 provided for a linear relationship between phosphor distribution and luminous intensity. The aim was to solve for the distribution function ρ from the luminous intensity Φ at the boundary. Since direct solution was not possible, a sparse regularization scheme was employed by minimizing the following object function.

$$\min \ \left\| \mathbf{A}\rho - \Phi \right\|_2^2 + \lambda \left\| \rho \right\|_1 \tag{1-6}$$

The experimentation was done with different view numbers, noise distortions and regularization parameters. Three cylindrical phantoms of height 20 cm and diameter 20 cm were used in the experiment with different location of nanophosphor in each one of them. The reconstruction levels were reported to be comparable to Bioluminescent Tomography and Fluorescent Molecular Tomography. The single pixel mode (discussed earlier) was found to be superior in creating an accurate description of distribution as compared to the cone beam scheme. But there was a manifold gain in terms of scanning time with this methodology over the narrow beam single-pixel mode.

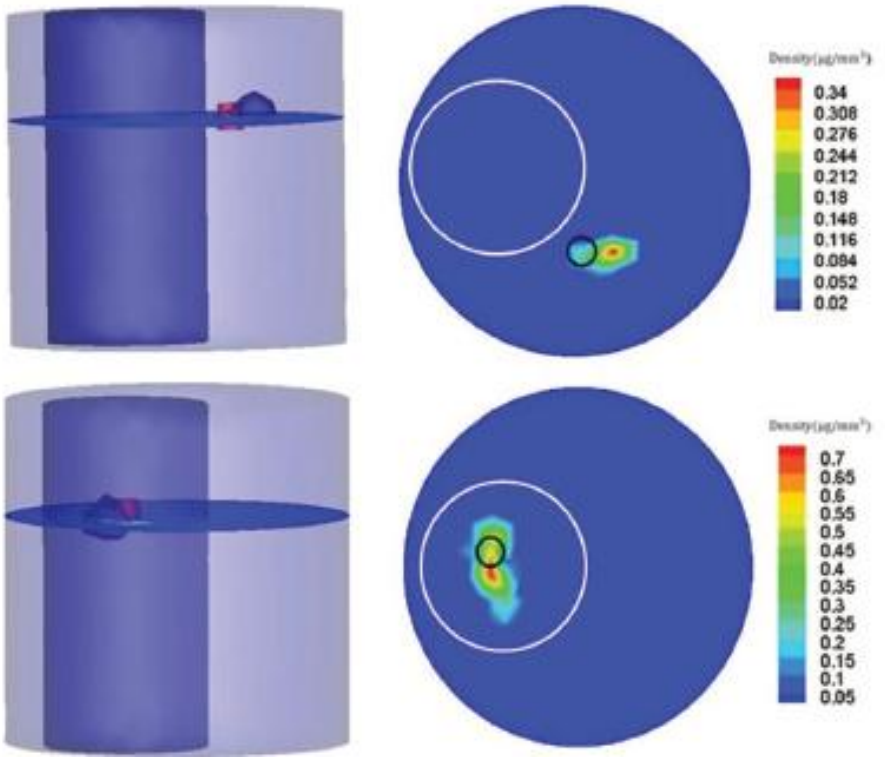

Figure 8: 3D Reconstruction of phantom in CB-XLCT
(Chen et.al, MPH **40**(3), 2013. Colored region shows reconstruction, circled region indicates the actual position of the sample of nanophosphor. Under Fair use 2013)

Efforts are still underway to improve the quality of X-ray Luminescent CT by implementing different schemes. Consideration of dose and nanophosphor distribution remains crucial as they are important towards safety of the subject. In the present consideration, these limitations pose a requirement of finding the best setting by means of finding an optimal balance between resolution, dose and noise.

METHODS

CHOICE OF SETTINGS

In performing XLCT by narrow beam excitation, there is an intrinsic problem. A choice has to be made between maximizing resolution and minimizing noise. In selecting a narrow collimator window, good resolution can be obtained by introducing a thin X-ray beam sampling the phosphor distribution at a fine scale. However, the tradeoff encountered in such a situation is a high noise because thin beams imply lesser photons. In keeping the collimator width broader, noise could be lowered by sending more photons per beam. But that happens at the cost of higher blur and low resolution. Hence, one parameter of the image suffers when we choose a conveniently high value for the either parameter. An optimal setting in terms of noise and resolution is desirable to get images of high quality. Focus of the current study remained on finding a balance between aforementioned parameters, dose being assumed same in both cases.

IMAGING MODEL

Beer-Lambert's Law demonstrates that for X-ray beam, fluence rate at a depth *x* is given as,

$$I = I_0 e^{-\int_0^x \mu(x,\mathbf{E}).dx} \tag{2-1}$$

μ is the attenuation coefficient for a thin beam taking into accounts both absorption and Compton scatter and I_0 the initial fluence rate. When we have a beam traveling from source ($\boldsymbol{q_i}$) to radial position **r**, the beam fluence rate is,

$$I = I_0 e^{-\int_{qi}^{\mathbf{r}} \mu(x,\mathbf{E}).dx} \tag{2-2}$$

The sample is assumed to be consisting of homogenous material described by its X-ray linear attenuation coefficient for thin rays, energy absorption coefficients μ(**r, E**) & μ_{en}(**r, E**), optical absorption and scattering coefficients, where **r** is the radial coordinate and **E** is the X-ray energy. Energy transferred to ionized electrons at **r** as kinetic energy, by the i^{th} beam could be written as,

$$E_i(\mathbf{r}) = \left\{ \mu_{en} I_0 e^{-\int_{q_i}^{\mathbf{r}} \mu(x,\mathbf{E}).dx} \right\}.w_i(\mathbf{r}) \tag{2-3}$$

Window function ***w(r)*** has unity value for i^{th} beam. Distributed Nanophosphor concentration could be modeled by a 2D-function f(**r**), about a small volume centered on **r** in the slice**.** The phantom is irradiated by a specific number of beams and optical signal recorded simultaneously. For the concentration, we can deduce the number of photons emitted by rescaling the values from light emission in a bulk crystal of high purity. In such case, the photon flux density can be written as,

$$\phi(\mathbf{r}) = \left(\frac{f(\mathbf{r})}{\rho_b} \right) \grave{o}_b E_i(\mathbf{r}) = \left(\frac{f(\mathbf{r})}{\rho_b} \right) \grave{o}_b \left\{ \mu_{en} I_0 e^{-\int_{q_i}^{\mathbf{r}} \mu(x,\mathbf{E}).dx} \right\}.w_i(\mathbf{r}) \tag{2-4}$$

ϵ = 60 / KeV & ρ = 7.44 gm. /ml. (pure crystal density for GOSE). In such geometry, the light photon from a small volume d**r** is,

$$\phi(\mathbf{r}).d\mathbf{r} = \frac{f(\mathbf{r})}{\rho_b} \grave{o}_b E_i(\mathbf{r}).d\mathbf{r} \tag{2-5}$$

The fluence or mean number of photon getting detected from the volume of interest over an interval **τ** is given by the following expression.

$$y_i = Q_E \left[\tau \int_{\Omega} s(\mathbf{r}) \phi_i(\mathbf{r}) d\mathbf{r} \right] \tag{2-6}$$

We assumed Q_E , the quantum efficiency of detector as unity, Ω the volume enclosing the sample and ***s(r)*** being the optical sensitivity map i.e. the probability of the photon getting detected by at least one of the photo detectors. ρ_s, the sample density is taken to be 1µg/ml with the background set 0.1 µg. / ml. We have taken into account beam widening due to Compton scatter of electrons and subsequent charge creation leading to photon generation from the neighborhood of the beam's path, by introducing parameters for thin beams.

RECONSTRUCTION MODEL

Emission Tomography, as is the case of X-ray Luminescent CT, follows a statistical nature of emission. There are several factors which could be attributed to the phenomenon. A given concentration of phosphor doesn't produce the exact same quantity of emission always and number of photons detected has a stochastic nature. Since detector is of finite extent, it isn't possible to collect all the emitted radiation. Lastly and most significantly, weak signals emitted by the trace element imply a high noise value, as compared to transmission tomography (conventional X-ray CT).

For our requirements in reconstructing XLCT data, Maximum Likelihood Estimation Maximization (MLEM) was an ideal candidate. ML-EM is an iterative solver which estimates

model parameters and produces an optimal solution, if not the most accurate to end with. The quality of reconstruction is good and taken to be a method of choice for emission tomography. A significant advantage of ML-EM technique over many other techniques is that it doesn't involve computation of gradients and converges to a non-negative optimal solution.

In the experiment, there were three classes of data: *observed* data being the set of detector readings, *unobserved* data being photon emission activity, which follows a Poisson nature and *model parameters* being the tissue properties. There is a many-to-one mapping with our current understanding, with observed reading being responsible for unobserved data, model parameter or a combination of both. In the ML-EM technique, reconstructions were started with initial settings of Maximum Likelihood and proceed to Expectation Maximization. It can be thought of as putting forward an initial guess of the data from current estimate and model and optimizing the guess by unobserved data.

The nanophosphor distribution is approximated in the Cartesian space by a set of N basis function $e_j(\mathbf{r})$ given as,

$$f(\mathbf{r}) = \langle \mathbf{x} \mid e(\mathbf{r}) \rangle = \sum_{j=1}^{N} x_j e_j(\mathbf{r}) \tag{2-7}$$

If the mean number of photons detected is **y**, it could be taken as a linear combination of phosphor concentration **x** and **A**, as given by **y = A.x** (2-8)

To evaluate the coefficients of matrix **A** we consider equation (2-6),

$$\begin{aligned} y_i &= \tau Q_E \int_{\Omega} s(\mathbf{r})\phi_i(\mathbf{r})d\mathbf{r} \\ &= \tau Q_E \int_{\Omega} s(\mathbf{r}) \frac{f(\mathbf{r})}{\rho_b} \grave{\alpha}_b E_i(\mathbf{r})d\mathbf{r} \\ &= \frac{\grave{\alpha}_b}{\rho_b} s_j \tau Q_E \int_{\Omega} f(\mathbf{r})E_i(\mathbf{r})d\mathbf{r} \\ &= \sum_j \left(\frac{\grave{\alpha}_b}{\rho_b} s_j \tau Q_E \int_{\Omega, j} e_j(\mathbf{r})E_i(\mathbf{r})d\mathbf{r} \right) x_j = \sum_j a_{ij} x_j \end{aligned} \tag{2-9}$$

Therefore, coefficients of **A** can be stated as,

$$a_{ij} = \frac{\tau \grave{\alpha}_b}{\rho_b} s_j \int_{\Omega} E_i(\mathbf{r})e_j(\mathbf{r})d\mathbf{r} \tag{2-10}$$

Here, $\boldsymbol{s_j}$ is the discrete optical sensitivity map i.e. $s(\mathbf{r}) = \{s(r_j)\}$. Measurements contribution **m** to the ML-EM over P beams, are statistical realizations of vector **Y** having independent components Y_i following Poisson distribution with mean $\boldsymbol{y_i}$, such that,

$$p_m(y) = \frac{e^{-y} y^m}{m_i!} \tag{2-11}$$

For a set of values recorded at the detector, we could elaborate

$$p_m(y_1, y_2 \ldots y_p) = \frac{e^{-y_1} y^{m_1}}{m_1!} \cdot \frac{e^{-y_2} y^{m_2}}{m_2!} \ldots \frac{e^{-y_P} y^{m_P}}{m_P!} \tag{2-12}$$

The log-likelihood of the above could be written as,

$$\log\ p_m(\mathbf{y}) = \sum_{i=1}^{P} -y_i + m_i \log(y_i) - \log(m_i!) \tag{2-13}$$

Ignoring the constant *m!* Factorial, vector **x** satisfying the ML criterion, is a solution to the function of **y**,

$$\max\ f_{\mathbf{m}}(\mathbf{y}) = \sum_{i=1}^{P} -y_i + m_i \log(y_i), \quad \mathbf{y} = \mathbf{A}\cdot\mathbf{x}\ \&\ \mathrm{x} \geq 0 \tag{2-14}$$

When **A** is a full-ranked matrix, the expression has a unique solution for $x \in \mathbb{R}^N$ *and* $y \in \mathbb{R}^P$. After ML step, EM was done iteratively following the scheme published by Shepp & Vardi [16] to reconstruct the data points. Expectation values of components of vector **m** can be written as,

$$E[m_i] = \sum_j m_i \frac{e^{y_j} {y_j}^{m_j}}{m_j!} \tag{2-15}$$

For n+1th iteration, m_i^{n+1} is written as follows

$$m_i^{n+1} = E[m_i \mid N_j {x_j}^n] = \frac{a_{ij} x_j}{N_j \sum_b a_{ib} x_b} \tag{2-16}$$

Applying minimization with respect to $\boldsymbol{x_i}$ in (2-14),

$$\begin{aligned} &\frac{\partial}{\partial x_j}\ \log P_{\mathbf{m}} = \sum_i -a_{ij} + \frac{m_i}{x_j} = 0 \\ &\Rightarrow {x_j}^{n+1} = \sum_i m_i a_{ij} \end{aligned} \tag{2-17}$$

Using (2-16) and (2-17), and writing the equation for x_j^n, successive estimates are done as,

$$x_j^{n+1} = \frac{x_j^n}{N_j} \sum_{i=1}^{P} a_{ij} \frac{m_i}{\sum_{b=1}^{N} a_{ib} x_b^n} \tag{2-18}$$

A sensitivity map which takes into non-uniform distribution of X-ray beam throughout the volume is given by,

$$N_j = \sum_{i=1}^{P} a_{ij} \tag{2-19}$$

The sensitivity map models the probability that photons which have been simulated to propagate by a Monte-Carlo technique, would land in a detector bin with reduced energy and contribute in image reconstruction. The sensitivity map depends on the coefficients a_{ij} of the activity matrix A. The value of sensitivity depends on sensitivity and position of detector, as well as scatter and attenuation. In calculating the sensitivity matrix, it is useful to consider circular symmetries to speed-up the imaging process. This sensitivity map could be determined by means of analytical expressions based on Radiative Transport Equations. But the technique is generally avoided since it is less accurate by several orders as compared to a Monte-Carlo simulation, even though it serves a computationally efficient closed-form technique.

SYSTEM DESIGN & METHODS IN SIMULATION

The XLCT simulation implemented selective excitation mechanism wherein target was irradiated by a sequence of narrow X-ray beams positioned at predefined locations and spacing. Photo-detectors were used in *single pixel* mode to measure fluence of optical photons diffusing out of the sample. For this mode, the data was summed from all detectors for a particular position of X-ray source. This method was effective since it could be assumed by principle that any optical activity detected occurred somewhere along the path of X-ray photons. It is well established that X-ray do not scatter as much as optical photons and hence the information was localized and optical sensor was not required to spatially resolve the information collected. Because nanophosphor was expected to be in small concentrations, high energy electrons created by Photoelectric effect and Compton scatter, contributing to photon creation, were supposed to be arising from tissue and not background. A small number of photons and subsequent data could be used to reconstruct high quality images. By using a *translate-rotate* scheme akin to first generation CT, images could be reconstructed without the need to spatially resolve the information at the detector.

The scanning X-ray source and optical detectors in the simulation were mounted at orthogonal directions. An additional X-ray detector could be positioned opposite to the source to simultaneously acquire X-ray tomographic projections. The current simulation however concentrated on the optical reconstruction. The nanophosphor characteristics simulated was based on Gd_2O_2S: Eu^{2+} with a density of $\rho = 7.44$ gm. /ml. This crystal in pure form responds with light emission of 60 photons/ KeV in the NIR spectrum (wavelength dependent on doping).

The phosphors are well-suited to for *in-vivo* imaging if coated with biocompatible agents. Mono-energetic beam of 100 KeV was used in the simulation.

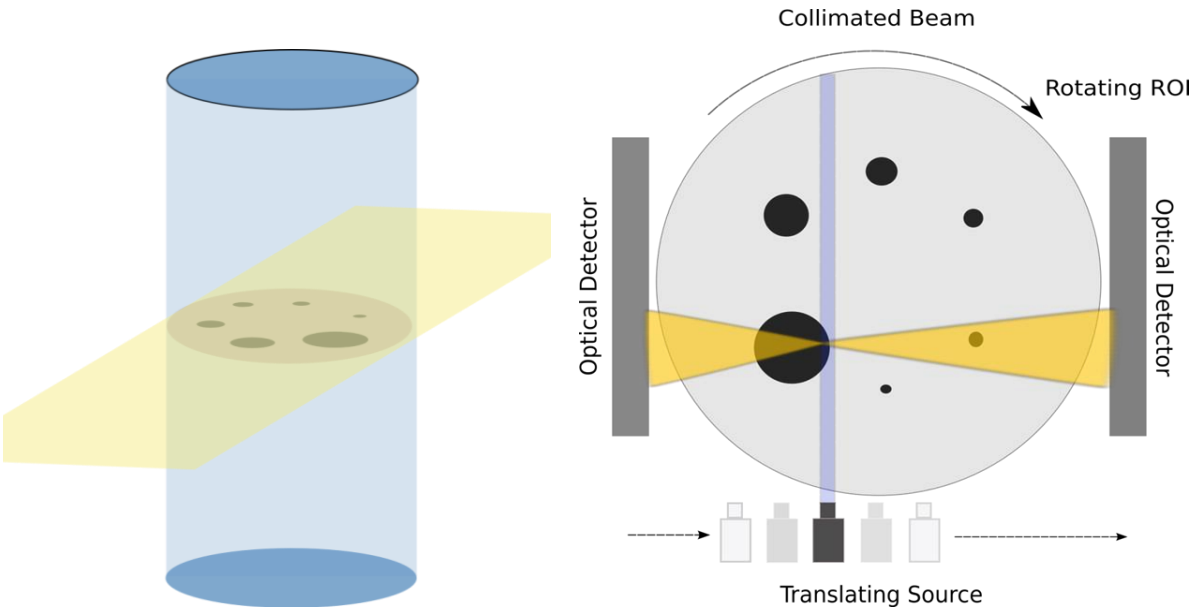

Figure 9: Model used in current XLCT simulation

X-ray undergoes inelastic Compton scatter and photoelectric absorption on interaction with matter. A Monte-Carlo simulation can effectively model the distribution of ionized charges created by X-ray interaction with matter[17]. The assumption used in this case is photons are launched with unity power (P=1W) within an infinite region with no boundaries. It holds valid if setup is designed such that detectors are placed very close to the boundary, accommodating only negligible air gap. The medium offers attenuation, absorption and scattering. Steady state distribution of the fluence rate in this case can be effectively determined.

In the simulation a known number of photons are launched, each with weightage initially set to 1. The photons undertake several steps in interacting with the tissue. The steps are based on the

probability of photon's movement before interaction by absorption and scattering. During each step as the photon propagates, it deposits a fraction of its energy into the local bins at the position. Each bin the array of bins accumulates photon weights deposited due to absorption by all the photons in that bin. After all photons have propagated, each bin contains an accumulated weight of absorbed photons. Dividing each bin by the total number of photons and volume of that particular bin yields the concentration of absorbed photons. Dividing it further by the absorption coefficient μ_a [cm^{-1}] yields the relative fluence rate. The array of bins for the package is organized as a function of distance *r* from the source, described usually in 3-dimensional geometries.

The distribution is converted to optical light by (2-4). The Monte Carlo method models the contribution of X-ray scattering to the total ionization and emission and compensates for beam widening due to scatter. This package simulates a specific number of photons (10^6), number of bins in the detector (100) and width of each bin (0.005cm) and the extent of width spatially. The optical properties are considered by taking into account absorption coefficient ($\mu_a = 0.1cm^{-1}$), scattering coefficient ($\mu_s = 100cm^{-1}$) and anisotropy (g = 0.90), which is the mean cosine of the angles of scattering.

The simulates experiment assumes a cylindrical phantom of 45 mm size in a Field of View (FOV) of 50 mm. The phantom is composed of 6 spheres of diameter 0.25mm, 0.5mm, 1mm, 2mm, 4mm and 8mm having a phosphor concentration of 1µg/ml surrounded by a background containing 0.1µg/ml phosphor distribution. Such a phantom mimics a tumor which has a higher uptake than its background composed of tissue and extra-cellular fluid. The FOV was sampled

uniformly in intervals of 0.1mm in both height and width across 30 views covering 360^0, to produce a 500x500 image. Optical detectors were simulated to surround the FOV of 50mm with negligible air gap, avoiding undesirable attenuation. For each measurement recorded, Poisson noise centered about the mean value of reading and amounting to 5% of the value was added to account for electronic noise.

The simulations were carried out for increasing beam widths. The least beam width was for 1 unit of sample i.e. 0.1mm wide over 500 linear increments in FOV. The greatest beam width was 1 mm wide over 50 linear increments. All images were reconstructed by 30 iterations of ML-EM (with voxel size of 0.1mm). From the 3 dimensional matrices, middle slices were considered for all subsequent evaluation. The outputs were recorded as bitmaps. Complement images were recorded to better examine the quality of reconstruction.

The following chapter exhibits the results of reconstruction and examines various metrics associated with the reconstructed image.

RESULTS

A. SIMULATION OUTPUTS

Following pages have some representative results obtained by the simulation. A full list is given in Appendix A-1.

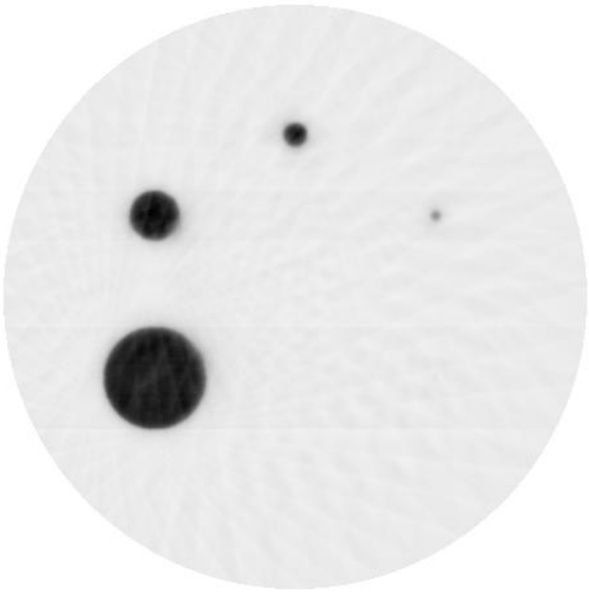

Output 1: 500 Sampling-points at 0.1mm width

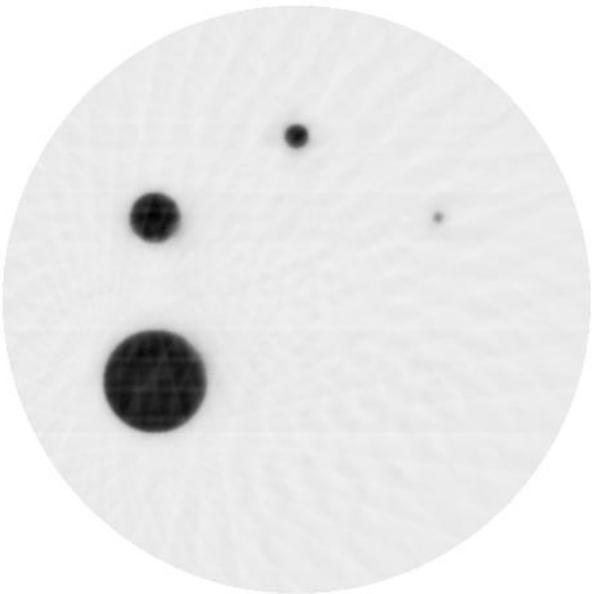

Output 2: 460 Sampling-points at 0.11mm width

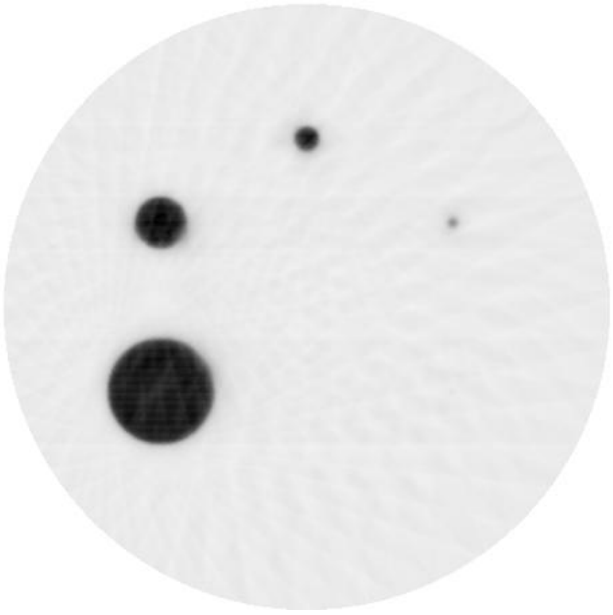

Output 3: 400 Sampling-points at 0.125mm width

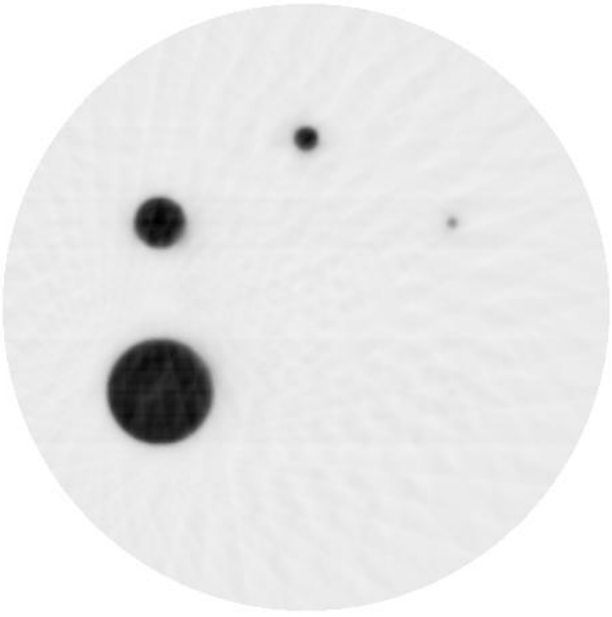

Output 4: 340 sampling points at 0.148mm width

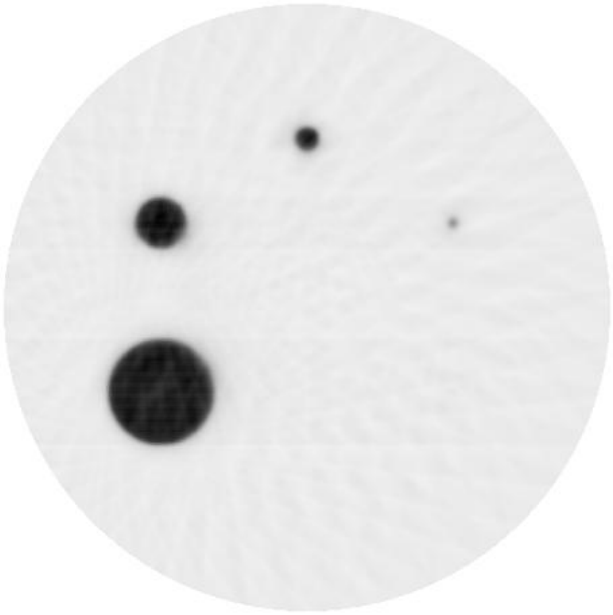

Output 5: 300 Sampling-points at 0.167mm width

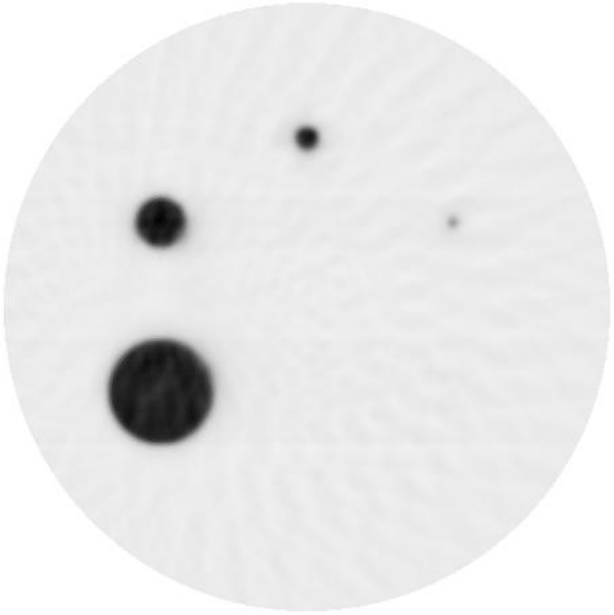

Output 6: 250 sampling points at 0.2mm width

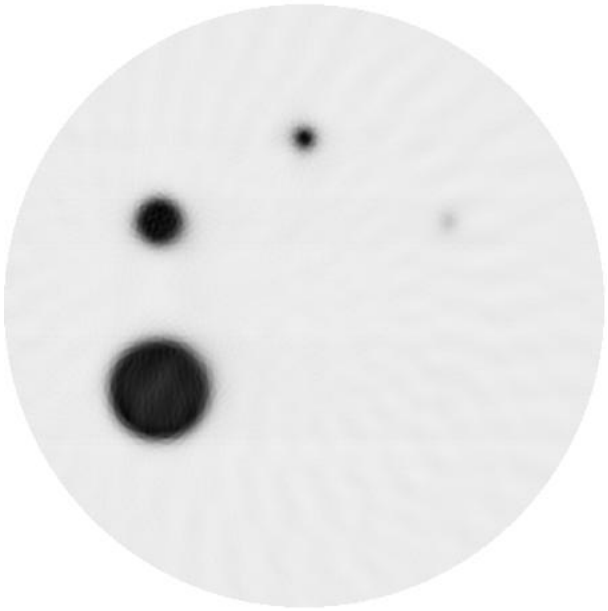

Output 7: 100 sampling points at 0.5mm width

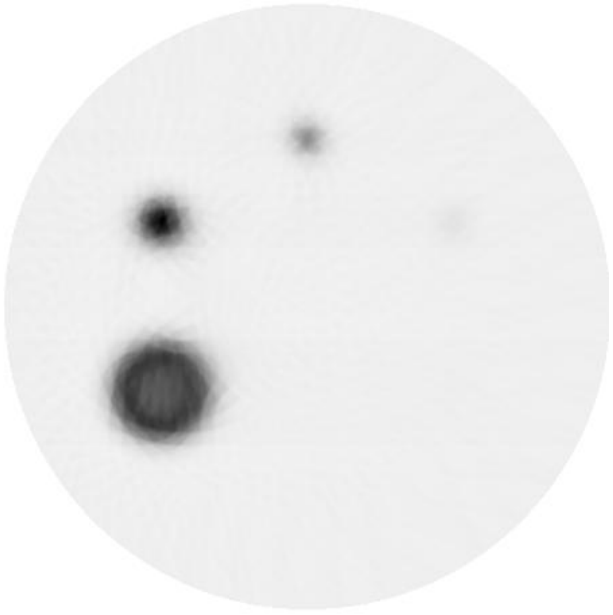

Output 8: 50 sampling points at 1.0 mm width

B. ANALYSIS

I. NOISE & SIGNAL TO NOISE RATIO (SNR)

Once the images were acquired, calculation of noise and signal to noise ratio was done. During the reconstruction, the image was recorded in a complement scheme. This was reverted by MATLAB's complement operation before doing SNR calculation. Four equal sized regions of extent 45x45 were selected, far removed from the nanophosphor distribution. The variance in the each of these four regions contributed to their individual standard deviation. A mean standard deviation was then calculated. To assess the quality of signal the mean value of a 45x45 region centered on the largest nanophosphor region was calculated. The reconstruction SNR can be expressed as,

$$\mathrm{Re}con - SNR = \frac{\mu_{sig}}{\sigma_{av}} \tag{3-1}$$

II. FULL WIDTH AT HALF MAXIMUM (FWHM)

The FWHM is an effective metric of resolution when line-pairs per mm. won't be possible with the scheme of imaging. The width of horizontal line profile, between 10% and 90% of maximum intensity change in an edge, is taken to be a working definition of resolution in many manuscripts. The sharpness of resolution depends on the extent of the blur. A perfect edge usually appears analogous to a step function in a line profile, whereas a gradual change is seen in the case of a blurred edge. More the blur, lesser is the resolution. In the experiment, a line profile of 50 points was taken across the edge. The FWHM (by the intensity change from 10% to 90% of the signal difference) was evaluated by a MATLAB script which was adaptive in accordance with the extent of blur. Any subjective bias was thus avoided.

III. TABULATED DATA.

The noise and SNR data have been reported in the following table.

Sampling (pts.)	μ_{sig}	σ	SNR
500	32.5014	1.7163	18.9368
490	31.9112	1.7152	18.6235
480	31.3299	1.7147	18.2716
470	30.7056	1.7345	17.7026
460	33.8228	1.7014	19.5348
450	34.8762	1.7041	20.4660
440	32.4220	1.7108	18.9509
430	35.7793	1.6755	21.3548
420	34.9963	1.6889	20.7213
410	33.0950	1.6978	19.4933
400	32.8403	1.6981	19.3389
380	35.4088	1.6605	21.3242
360	35.7713	1.6637	21.5012
340	31.5213	1.6664	18.9155
320	31.9305	1.6482	19.3727
300	33.5321	1.6219	20.6747
280	33.8464	1.6178	20.9212
260	34.8719	1.5947	21.8673
250	32.2859	1.5586	21.6773
240	33.7741	1.5427	21.8926
220	33.8729	1.5241	22.2246
200	34.2306	1.4907	22.9627
180	35.5416	1.4551	24.4255
167	34.3601	1.4332	23.9744
160	32.2004	1.4156	22.7472
140	29.6328	1.3792	21.5794
125	34.7552	1.3148	26.4338
120	36.4490	1.2809	28.4557
100	34.4112	1.2184	28.2432
80	38.9149	1.0842	35.8927
60	53.1333	0.9040	58.7738
50	74.6115	0.8257	90.3577

Table 2: Noise and SNR values in reconstruction

The Full Width at Half Maximum are tabulated as follows,

Sampling (pts.)	FWHM
500	2.71
490	2.88
480	2.84
470	2.65
460	2.07
450	2.92
440	2.82
430	2.87
420	2.93
410	2.95
400	2.91
380	2.99
360	3.61
340	3.52
320	4.18
300	3.81
280	4.59
260	4.34
250	4.17
240	4.70
220	4.73
200	5.46
180	5.96
167	6.06
160	6.20
140	7.29
125	7.48
120	7.91
100	10.07
80	14.57
60	14.15
50	18.33

Table 3: FWHM values evaluated post-reconstruction.

Variation of SNR and FWHM is shown in the following plots.

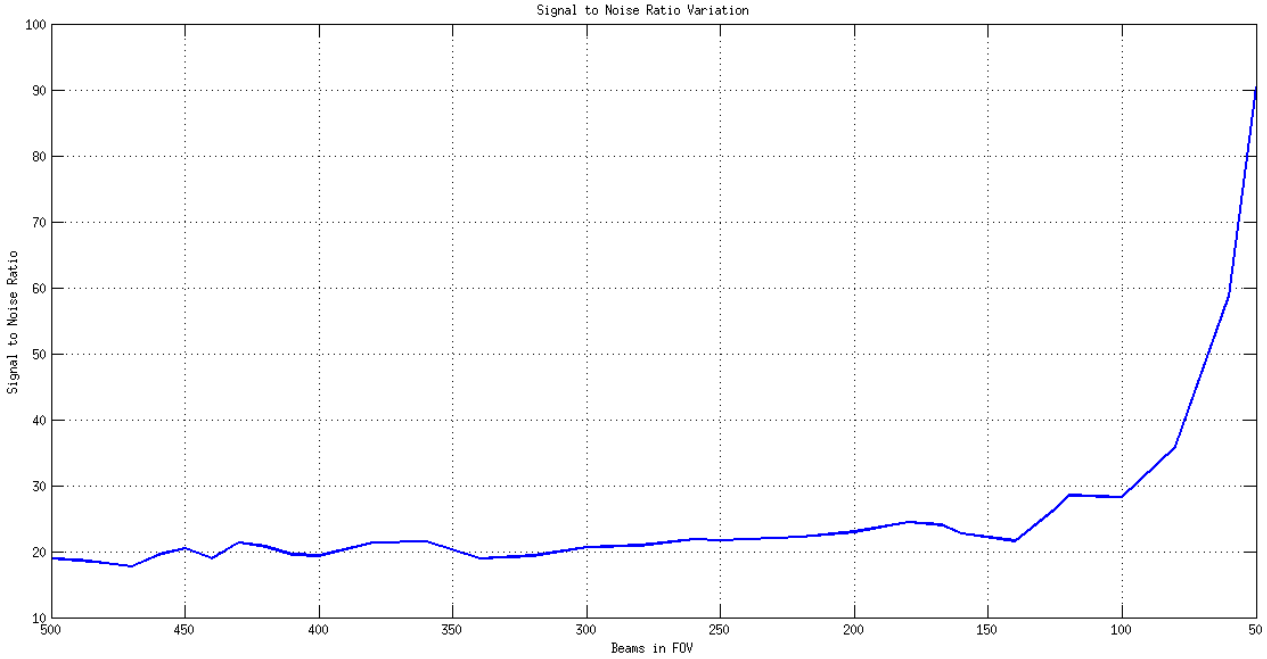

Figure 10: Variation of SNR in reconstruction

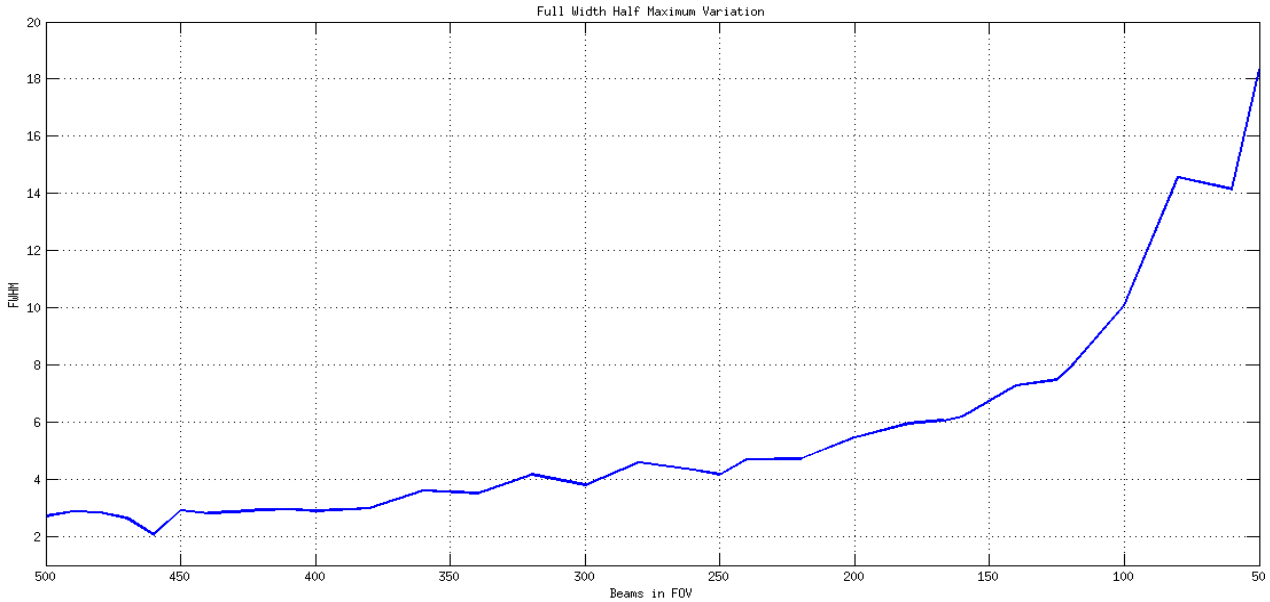

Figure 11: Variation of FWHM in reconstruction

DISCUSSION

WANG-BOVIK QUALITY INDEX

The values and plot of Noise and FWHM do not directly indicate presence of an optimality criterion. Hence quality indices are employed, the first of which is described.

Given two images a & b, let $\bar{a}$ denote the mean of a, $\bar{b}$ denote mean of b, $\sigma_a^{\,2}$ and σ_b^2 denote variances in a & b, and σ_{ab} denote covariance between a & b respectively. These quantities can be expressed conveniently like the following expressions,

$$\sigma_a^{\,2} = \frac{1}{MN-1}\sum_{m=1}^{M}\sum_{n=1}^{N} \left[a(m,n)-\bar{a}\right]^2 \tag{4-1}$$

$$\sigma_{ab} = \frac{1}{MN-1}\sum_{m=1}^{M}\sum_{n=1}^{N} \left[a(m,n)-\bar{a}\right]\left[b(m,n)-\bar{b}\right] \tag{4-2}$$

We define a quantity Q_0, as follows,

$$Q_0 = \frac{4\sigma_{ab}\bar{a}\bar{b}}{\left(\bar{a}^2+\bar{b}^2\right)\left(\sigma_a^{\,2}+\sigma_b^{\,2}\right)} = \frac{\sigma_{ab}}{\sigma_a\sigma_b}\cdot\frac{2\bar{a}\bar{b}}{\bar{a}^2+\bar{b}^2}\cdot\frac{2\sigma_a\sigma_b}{\sigma_a^2+\sigma_b^2} \tag{4-3}$$

Wang, Bovik et.al, propose this as a universal image quality index, which describes the level of distortion between two input images [18, 19]. It could also be represented as Q_0 (a, b). It evaluates the similarity of images, taking on values between -1 and 1. Unity would indicate perfect match between two images. The first term in the expanded expression is the geometrical correlation between the two images. The second term describes the luminous distortion between candidate images, by taking a value in [0, 1]. The third factor indicates contrast distortion between the images by taking on a value in [0, 1]. Wang Bovik index is a good technique for

comparing images. It scores over Mean Square Error technique, which innately emphasizes the energy component only rather than comparing geometrical and luminous distortion.

Considering that pixel intensity distribution is a non-stationary process, we can choose a convenient window size and averaging the indices over the traversing window to yield a single numeric representation.

$$Q_0(a,b) = \frac{1}{|W|} \sum_{w \in W} Q_0(a,b \mid w) \tag{4-4}$$

The window size was chosen to be 7x7 and incrementing over the image in 1 pixel increments. Windowing approach is better than considering, because it amplifies the local distortion in a small neighborhood and fine differences could be evaluated. The reference was taken to be a slice image of the original phantom which is being imaged and reconstructed.

MODIFIED WANG-BOVIK QUALITY INDEX

The Wang Bovik Index pertains to the distortion of the image. However, it is a composite of pixel value covariance, luminous distortion and contrast distortion. The index, even if robust doesn't take into account the point-spread function (PSF). Modification of the metric to factor in the PSF by including Full-Width Half Maximum would introduce contribution of resolution to the overall image quality. A modified scheme is proposed herein, where the quality index is divided by the Full-Width Half Maximum (FWHM). Since a lower FWHM would indicate a higher quality, the inclusion appears in denominator. The modified index is represented as

$$Q' = \frac{Q_0(a,b)}{\rho_a} \tag{4-5}$$

The Wang-Bovik Quality factor and the modified version are tabulated in the following table.

Sampling (points in FOV)	Wang-Bovik Index Q_0	Modified Q_0
500	0.9118	0.33646
490	0.9124	0.31681
480	0.9124	0.32127
470	0.9124	0.34430
460	0.9106	0.43990
450	0.9090	0.31130
440	0.9118	0.32333
430	0.9089	0.31669
420	0.9081	0.30993
410	0.9098	0.30841
400	0.9099	0.31268
380	0.9074	0.30348
360	0.9069	0.25122
340	0.9083	0.25804
320	0.9077	0.21715
300	0.9059	0.23777
280	0.9047	0.19710
260	0.9038	0.20825
250	0.9030	0.21655
240	0.9023	0.19198
220	0.9014	0.19057
200	0.8986	0.16458
180	0.8970	0.15050
167	0.8964	0.14792
160	0.8944	0.14426
140	0.8948	0.12274
125	0.8879	0.11870
120	0.8842	0.11178
100	0.8774	0.08713
80	0.8608	0.05908
60	0.8169	0.05773
50	0.7471	0.04076

Table 4: Quality Indices (Q_0 and Modified Q_0)

A plot of the modified Wang-Bovik index is shown. A peak is seen in the beam width of ~0.11mm. It is an indicator of optimality in terms of maximum covariance, and minimum luminous and contrast distortion.

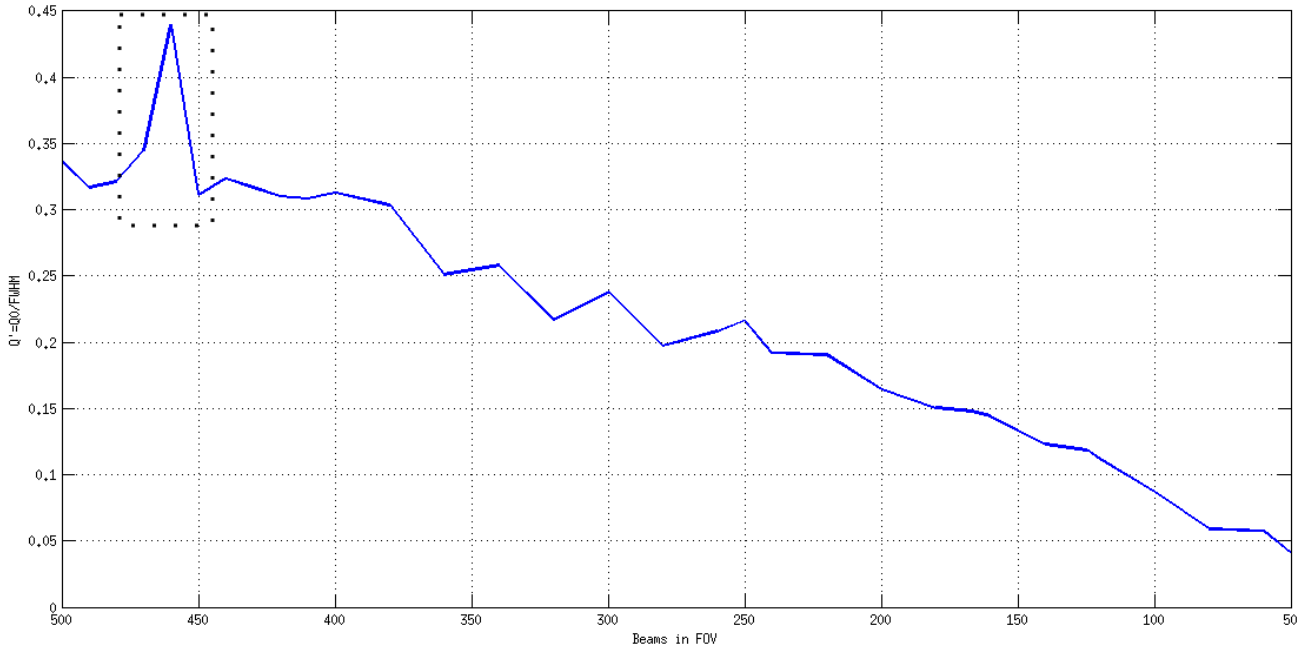

Figure 12: Modified Wang-Bovik Index. Optimality indicated by the peak

CT FIGURE OF MERIT

To independently investigate the result from preceding modified Wang Bovik Quality factor, another method of assessment was employed. As proposed in *Computed Tomography* by W.A. Kalender, a figure of merit can be devised which taken in account noise, dose and spatial resolution [20]. A figure of merit proposed is

$$Q = \frac{c}{\sigma^2 M^{-4} D} \tag{4-6}$$

Noise is represented as σ, and dose by D per unit volume. M denoted the 10% MTF expressed in inverse of length. If we consider FWHM (ρ) in dimensions of length, the expression can be re-written as,

$$Q = \frac{k}{\sigma^2 \rho^4 D} \tag{4-7}$$

When we consider introducing a fixed number of X-ray photons into the thin beam profile, we can express dose D per unit volume in the reconstructed images as,

$$D \propto \frac{N}{\rho^3} \tag{4-8}$$

Hence,

$$Q \propto \frac{k}{\sigma^2 \rho^4 \left(\frac{N}{\rho^3} \right)} \tag{4-9}$$

Or,

$$Q \propto \frac{k'}{\sigma^2 \rho} \tag{4-10}$$

The quality of image is inversely proportional to the square of noise and FWHM. The lower the value of the term $\sigma^2 \rho$, the better is the quality of image considering both noise and resolution (in terms of FWHM). Finding the minima in a plot would correspond to the image with optimum set of parameters. We plot $\sigma^2 \rho$ variation in the graph shown in the following page. As can be seen, a global minimum is observed in the value corresponding to approximately 0.11 mm beam width (i.e. at 460 beams in FOV).

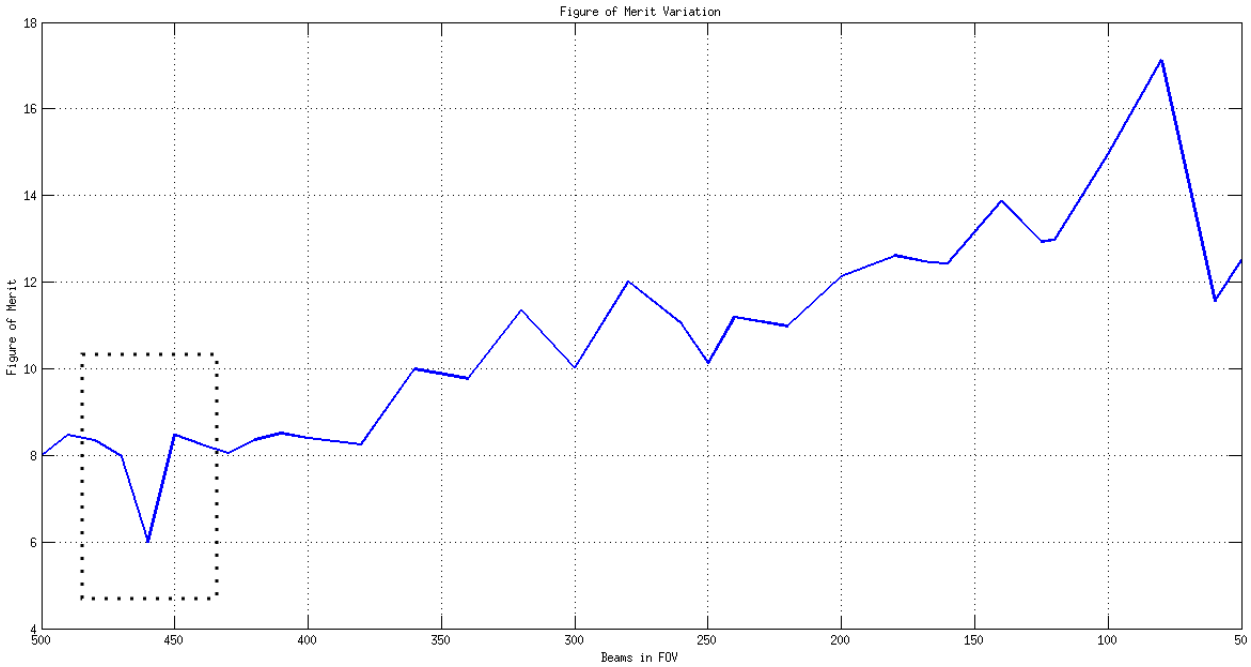

Figure 13: Variation in Figure of Merit. Minimal value indicated in figure

As seen with the plots, best results don't occur when the sampling beam getting thinner. There is a point of optimum performance which is achieved. Deviating from that optimum point leads to reduced performance. When the beam is thicker, higher FWHM leads to a poor image quality. But when we keep reducing the beam width, we reach a point where performance characteristics are maximized. Thinning the beam beyond this point doesn't improve the resolution because of X-ray scattering. Noise may also keep increasing, consequently leading to lower performance.

CONCLUSION

The study has focused on the material feasibility, system design and simulation of X-ray Luminescent CT. Significant recent advances in Positron Emission Tomography (PET)[21], Optical imaging[22], Single positron emission computed tomography (SPECT) and Magnetic Resonance Imaging (MRI)[23] have invigorated research into molecular markers. The approach has been already applied to numerous pathologies[24], to determine efficacy via apoptosis markers and to identify cancers and tumors[25]. Incorporation of these molecular markers has had a profound impact in the current imaging research. X-ray Luminescent CT is an upcoming modality utilizing such markers, which should soon be adopted into the mainstream imaging. Though it might be limited to animal studies and interventional procedures, combining the accuracy of CT process and sensitivity of molecular imaging researchers would have a novel tool in detecting and staging various abnormalities.

In this study, the focus was on finding a paradigm which would enable us to find an optimal setting suitable for imaging. Because of the high stakes involved through large exposure, high dosage and long scanning times, it is prudent to have prior information about scan settings which would lead to the best quality of images. Once these pre-clinical settings are known, the aperture size can be adjusted minimizing the costs and risks involved in conducting high-valued experiments.

The study aimed at establishing an imaging model and reconstruction method for X-ray Luminescent Computed Tomography. The imaging model was discussed extensively and the choice of Maximum Likelihood Estimation – Expectation Maximization (MLEM) was studied

thoroughly. It corroborated the results of studies done earlier in other research institutions. Further, it was justified as to why a need for optimal settings was required.

Simulations proceeded through selecting various values of aperture thickness. The beam thicknesses were varied between 0.1 mm to 1.0 mm. Each simulation was reconstructed with the exact same system settings, the only difference being the beam width of aperture. Through standardizing the acquisition and reconstruction, an ideal beam width of 0.11 mm could be identified, which occurred with the Field of View getting scanned by 460 thin X-ray pencil beams. This setting corresponded to the perfect balance between FWHM and reconstruction noise, yielding the best result. Any width higher than this didn't further improve resolution but increased noise due to scatter becoming dominant. Higher aperture sizes led to poor resolution in images and consequently poor quality.

The optimal criterion was identified by two separate quality metrics, which were independent of each other. Both Modified Wang-Bovik index and CT Figure of Merit pointed to the same value of optimality, reinforcing the finds of the study. The study hopes to serve in establishing a useful and convenient paradigm where the system design differs from the one which this experimental study describes.

In establishing XLCT as a frontline tool in investigative research many milestones still need to be crossed. Improvements such as radiation resilient CCD camera, higher sensitivity of molecular markers, exponential increases in the quantum efficiency of nanophosphors and reduced scanning time could only bring down the costs associated with the design and operation

of this modality. A promising direction which holds new avenues in improvement is in perfecting the Cone beam based X-ray Luminescent Computed Tomography approach. This paradigm would not only utilize the X-ray energy more efficiently through the cone-beam, but also remove the deficiencies of using narrow beam methodology – lengthy duration of scans and computation intensive reconstruction. The challenge in achieving this objective remains in making highly accurate photon propagation and X-ray scattering models, which are material specific.

With the novelty this modality has introduced, its future should see lot of improvements. Application of XLCT to high quality research studies and image guided intervention can be envisioned in near future. In this context, optimization techniques for this modality would always hold valuable position in the imaging landscape.

REFERENCE

1. Alivisatos, A.P., *Semiconductor clusters, nanocrystals, and quantum dots.* Science, 1996. **271**(5251): p. 933-933.
2. Cai, W. and X. Chen, *Nanoplatforms for Targeted Molecular Imaging in Living Subjects.* Small, 2007. **3**(11): p. 1840-1854.
3. Maeda, H., et al., *Tumor vascular permeability and the EPR effect in macromolecular therapeutics: a review.* Journal of Controlled Release, 2000. **65**(1–2): p. 271-284.
4. Tanaka, T., et al., *Tumor targeting based on the effect of enhanced permeability and retention (EPR) and the mechanism of receptor-mediated endocytosis (RME).* International Journal of Pharmaceutics, 2004. **277**(1–2): p. 39-61.
5. Tian, Y., et al., *Preparation and luminescence property of Gd_2O_2S:Tb X-ray nano-phosphors using the complex precipitation method.* Journal of Alloys and Compounds, 2007. **433**(1–2): p. 313-317.
6. Xing, M.M., et al., *Preparation and characterization of monodisperse spherical particles of X-ray nano-phosphors based on Gd_2O_2S:Tb.* Chinese Science Bulletin, 2009. **54**(17): p. 2982-2986.
7. Rajan, K.G. and A.J. Lenus, *X-ray excited optical luminescence studies on the system BaXY (X,Y=F, Cl, Br, I).* Pramana, 2005. **65**(2): p. 323-338.
8. Issler, S.L. and C.C. Torardi, *Solid state chemistry and luminescence of X-ray phosphors.* Journal of Alloys and Compounds, 1995. **229**(1): p. 54-65.
9. Chen, W., et al., *The origin of x-ray luminescence from CdTe nanoparticles in CdTe/BaFBr : Eu2+ nanocomposite phosphors.* Journal of Applied Physics, 2006. **99**(3): p. 034302-034302-5.

10. Pratx, G., et al., *Tomographic molecular imaging of x-ray-excitable nanoparticles.* Opt. Lett., 2010. **35**(20): p. 3345-3347.

11. Pratx, G., et al., *X-Ray Luminescence Computed Tomography via Selective Excitation: A Feasibility Study.* Medical Imaging, IEEE Transactions on, 2010. **29**(12): p. 1992-1999.

12. Hounsfield, G.N., *Computerized transverse axial scanning (tomography): Part 1. Description of system.* British Journal of Radiology, 1973. **46**(552): p. 1016-1022.

13. Shepp, L.A. and B.F. Logan, *The Fourier reconstruction of a head section.* IEEE Trans. Nucl. Sci, 1974. **21**(3): p. 21-43.

14. Carpenter, C.M., et al., *Hybrid x-ray/optical luminescence imaging: Characterization of experimental conditions.* Medical Physics, 2010. **37**(8): p. 4011-4018.

15. Chen, D., et al., *Cone beam x-ray luminescence computed tomography: A feasibility study.* Medical Physics, 2013. **40**(3): p. 031111-14.

16. Shepp, L.A. and Y. Vardi, *Maximum Likelihood Reconstruction for Emission Tomography.* Medical Imaging, IEEE Transactions on, 1982. **1**(2): p. 113-122.

17. Jacques, S.L., *Light distributions from point, line and plane sources for photochemical reactions and fluorescence in turbid biological tissues.* Photochemistry and photobiology, 1998. **67**(1): p. 23-32.

18. Zhou, W. and A.C. Bovik, *A universal image quality index.* Signal Processing Letters, IEEE, 2002. **9**(3): p. 81-84.

19. Piella, G. *New quality measures for image fusion*. in *Proceedings of the Seventh International Conference on Information Fusion*. 2004.

20. Kalender, W. and K.O. Khadivi, *Computed tomography: Fundamentals, system technology, image quality, applications.* Medical Physics, 2006. **33**: p. 3076.

21. Gambhir, S.S., *Molecular imaging of cancer with positron emission tomography.* Nature Reviews Cancer, 2002. **2**(9): p. 683-693.

22. Pogue, B.W. and M.S. Patterson, *Review of tissue simulating phantoms for optical spectroscopy, imaging and dosimetry.* Journal of biomedical optics, 2006. **11**(4): p. 041102-041102-16.

23. Pham, T.H., et al., *Broad bandwidth frequency domain instrument for quantitative tissue optical spectroscopy.* Review of Scientific Instruments, 2000. **71**(6): p. 2500-2513.

24. Weissleder, R. and V. Ntziachristos, *Shedding light onto live molecular targets.* Nature medicine, 2003. **9**(1): p. 123-128.

25. Blankenberg, F.G., *In vivo detection of apoptosis.* Journal of Nuclear Medicine, 2008. **49**(Suppl 2): p. 81S-95S.